

A Compton imaging detection system for neutron resonance capture analysis at Back-n

Jin-Cheng Wang(王金成), Jie Ren(任杰), Wei Jiang(蒋伟), Suyalatu Zhang(张苏雅拉吐), Ping Cao(曹平), Xichao Ruan(阮锡超), Hao-Lan Yang(杨皓岚), Jie-Ming Xue(薛洁明), Ying-Yi Liu(刘颖一), Jie Bao(鲍杰), Guang-Yuan Luan(栾广源), Qi-Wei Zhang(张奇玮), Yi-Jia Qiu(邱奕嘉), Yong-Hao Chen(陈永浩), Rui-Rui Fan(樊瑞睿), Wei-Yu Wang(王维宇), Zhen-Yu Sun(孙振宇), De-Xin Wang(王德鑫), and Mei-Rong Huang(黄美容)
Citation: Chin. Phys. B, 2026, 35 (**8**): 080703. DOI: 10.1088/1674-1056/ae15f7
http://cpb.iphy.ac.cn; http://iopscience.iop.org/cpb

What follows is a list of articles you may be interested in

Physics-informed neural network for material identification via distortion-robust polychromatic x-ray attenuation correction in photon-counting detectors

Xin Yan(闫欣), Jie Zhang(张杰), Kai He(何凯), Yiheng Liu(刘毅恒), Yuetong Zhao(赵悦彤), Gang Wang(王刚), Xinlong Chang(常新龙), and Youwei Zhang(张有为)
Chin. Phys. B, 2026, 35 (**5**): 050702. DOI: 10.1088/1674-1056/ae5a13

Measurement of the relative neutron sensitivity curve of a $LaBr_3(Ce)$ scintillator based on the CSNS Back-n white neutron source

Jian Liu(刘建), Dongming Wang(王东明), Yuecheng Fu(甫跃成), Zhongbao Li(李忠宝), Han Yi(易晗), and Longtao Yi(易龙涛)
Chin. Phys. B, 2023, 32 (**10**): 100703. DOI: 10.1088/1674-1056/acca08

Direct measurement of an energy-dependent single-event-upset cross-section with time-of-flight method at CSNS

Biao Pei(裴标), Zhixin Tan(谭志新), Yongning He(贺永宁), Xiaolong Zhao(赵小龙), and Ruirui Fan(樊瑞睿)
Chin. Phys. B, 2023, 32 (**2**): 020705. DOI: 10.1088/1674-1056/aca603

X-ray focusing using an x-ray lens composed of multi-square polycapillary slices

Kai Pan(潘凯), Tian-Cheng Yi(易天成), Zhao Wang(王曌), Mo Zhou(周末), Yu-De Li(李玉德), Zhi-Guo Liu(刘志国), Xiao-Yan Lin(林晓燕), and Tian-Xi Sun(孙天希)
Chin. Phys. B, 2022, 31 (**2**): 020701. DOI: 10.1088/1674-1056/ac381a

Study on γ-ray source from the resonant reaction $^{19}F(p,\alpha\gamma)^{16}O$ at E_p=340 keV

Fu-Long Liu(刘伏龙), Wan-Sha Yang(杨婉莎), Ji-Hong Wei(魏继红), Di Wu(吴笛), Yang-Fan He(何阳帆), Yu-Chen Li(李雨尘), Tian-Li Ma(马田丽), Yang-Ping Shen(谌阳平), Qi-Wen Fan(樊启文), Chuang-Ye He(贺创业), Bing Guo(郭冰), Nai-Yan Wang(王乃彦)
Chin. Phys. B, 2020, 29 (**7**): 070702. DOI: 10.1088/1674-1056/ab96a0

A Compton imaging detection system for neutron resonance capture analysis at Back-n

Jin-Cheng Wang(王金成)[1,2], Jie Ren(任杰)[2,†], Wei Jiang(蒋伟)[3,4], Suyalatu Zhang(张苏雅拉吐)[5], Ping Cao(曹平)[6,7], Xichao Ruan(阮锡超)[2,‡], Hao-Lan Yang(杨皓岚)[2], Jie-Ming Xue(薛洁明)[2], Ying-Yi Liu(刘颖一)[2], Jie Bao(鲍杰)[2], Guang-Yuan Luan(栾广源)[2], Qi-Wei Zhang(张奇玮)[2], Yi-Jia Qiu(邱奕嘉)[3,4], Yong-Hao Chen(陈永浩)[3,4], Rui-Rui Fan(樊瑞睿)[3,4,8], Wei-Yu Wang(王维宇)[9,10], Zhen-Yu Sun(孙振宇)[11], De-Xin Wang(王德鑫)[5], and Mei-Rong Huang(黄美容)[5]

[1] *College of Science, Inner Mongolia University of Technology, Hohhot* 010051, *China*
[2] *Key Laboratory of Nuclear Data, China Institute of Atomic Energy, Beijing* 102413, *China*
[3] *Institute of High Energy Physics, Chinese Academy of Sciences (CAS), Beijing* 100049, *China*
[4] *Spallation Neutron Source Science Center, Dongguan* 523803, *China*
[5] *College of Physics and Electronic Information, Inner Mongolia University for Nationalities, Tongliao* 028000, *China*
[6] *State Key Laboratory of Particle Detection and Electronics, University of Science and Technology of China, Hefei* 230026, *China*
[7] *School of Nuclear Science and Technology, University of Science and Technology of China, Hefei* 230026, *China*
[8] *State Key Laboratory of Particle Detection and Electronics, Institute of High Energy Physics Chinese Academy of Sciences, Beijing* 100049, *China*
[9] *State Key Laboratory of Particle Detection and Electronics, University of Science and Technology of China, Hefei* 230026, *China*
[10] *Department of Modern Physics, University of Science and Technology of China, Hefei* 230026, *China*
[11] *Institute of Advanced Technology, University of Science and Technology of China, Hefei* 230031, *China*

(Received 29 August 2025; revised manuscript received 14 October 2025; accepted manuscript online 22 October 2025)

Neutron resonance capture analysis (NRCA) is a method that utilizes the resonance structures in neutron-induced reactions to determine the elemental composition of materials. It is used for the non-destructive analysis of cultural heritage objects, archaeological artifacts, and reference materials. The back streaming white neutron facility (Back-n) of the China Spallation Neutron Source (CSNS) provides neutron energy ranging from eV to MeV, offering favorable beam conditions for the development of neutron resonance capture imaging (NRCI). Compton imaging is applied to achieve NRCI in this work. A series of dedicated measurements with calibrated sources and with Back-n neutron beam incident on a ^{197}Au sample have been carried out. The results indicate that this detector can achieve NRCI at Back-n. This work provides a foundation for nuclide identification using NRCI at the Back-n facility.

Keywords: NRCA, Compton imaging, Back-n, $CeBr_3$, signal to background ratio

PACS: 07.85.Fv, 07.85.–m, 87.59.–e, 95.55.Ka

DOI: 10.1088/1674-1056/ae15f7 **CSTR:** 32038.14.CPB.ae15f7

1. Introduction

Neutron resonance capture analysis (NRCA) is based on the appearance of resonance peaks in the cross-section of neutron-induced reactions. Neutron radiative capture resonances are a characteristic of every isotope, which forms a useful "fingerprint" for identifying elements in the sample.[1–5] The approach relies on the recognition of elements through the resonance energies of neutrons exhibited in the radiative capture reaction (alternatively, via the transmission curve) and subsequently ascertaining the concentration of these elements by quantifying the detected yield of (n,γ) within these resonances (or equivalently, by measuring the resonance area on the transmission curve). At low neutron energies (1 eV to 1 keV), the resonances are distinctly spaced apart, with the average level distance D being significantly larger than their width Γ. The resonance region is specifically identified as the zone where the average level distance exceeds the average level width ($D > \Gamma$). In these energy regions, neutron resonance spectroscopy across a broad neutron energy spectrum is achieved utilizing the time-of-flight (TOF) method. The energies and intensities of these resonance peaks serve as indicators for identifying isotopes and quantifying their concentrations. Given the profound penetration of epithermal neutrons into matter, this technique enables the determination of bulk elemental compositions. Notably, the NRCA necessitates a pulsed neutron source,[1,2] differentiating it from conventional methods like neutron activation analysis[6,7] and prompt gamma activation analysis.[8,9] A comprehensive review of NRCA for non-destructive analysis is introduced in Refs. [1,2]. Cippo *et al.*[10] achieved spatial resolution in NRCA through tomographic imaging techniques.

This work reports a new detection system used at Back-n

†Corresponding author. E-mail: renjie@ciae.ac.cn
‡Corresponding author. E-mail: ruanxc@ciae.ac.cn

© 2026 Chinese Physical Society and IOP Publishing Ltd. All rights, including for text and data mining, AI training, and similar technologies, are reserved.

that implements both NRCA and imaging, which is known as neutron resonance capture imaging (NRCI).[10,11] By employing a dual-layer Compton camera, the system simultaneously achieves both Compton imaging and measurement of characteristic resonance peaks of isotopes. The dual-layer Compton camera architecture comprises a scatter detector layer and an absorption detector layer. When operated in time coincidence, this configuration enables the application of Compton scattering principles to derive information about the incident radiation direction. This detection system includes $CeBr_3$ crystals, silicon photomultipliers (SiPMs), and readout electronics. The testing experiments conducted at the back-streaming white neutron facility (Back-n) successfully identified resonance peaks in different energy regions ranging from eV to several tens of keV and achieved imaging of the ^{197}Au sample.

2. Methods

For material analysis utilizing resonance structures in neutron-induced reaction cross sections, it is crucial to have accurate information about the energy of the neutrons either detected or captured within the sample. Neutron resonance spectroscopy can be conducted across a wide range of neutron energies, either through the application of the TOF method or by utilizing quasi-monoenergetic neutrons generated by charged particle-induced reactions. In the case of the latter, the neutron energy can be adjusted by altering the energy of the interacting charged particle or the angle of emergence. Due to the restricted energy resolution, measurements employing a continuous quasi-monoenergetic neutron beam are inadequate for comprehensive elemental composition analysis. However, they can still be used for specific applications by transmission measurements in the high energy region, such as detecting explosives or assisting in diamond mining.[12] In NRCA, pulsed neutron beams must be employed in conjunction with time-of-flight techniques for neutron resonance spectroscopy. The advancement from NRCA to NRCI technology requires the additional integration of imaging capabilities in this work.

2.1. Neutron resonance capture analysis

In the neutron capture experiment, the measured quantity corresponds to the fraction of incident neutrons that interact with the sample and create a signal in the detection system. For non-fissionable nuclei at energies below the inelastic scattering threshold, this interaction fraction depends on both capture and elastic scattering probabilities. The capture (Y_c) and scattering yields (Y_n) per neutron can be expressed as a function of the Doppler-broadened total (σ_{tot}^D), capture (σ_γ^D), and scattering (σ_n^D) cross sections by[1,2]

$$Y_{c,k} = F(E) n_k \sigma_{\gamma,k}^D(E) + Y_{M,k}(E), \quad (1)$$

$$Y_{n,k} = F(E) n_k \sigma_{n,k}^D(E) + Y_{M,k}(E). \quad (2)$$

Here, n_k represents the areal number density of nuclide k, while Y_M incorporates the contribution from neutrons that undergo one or more scattering events prior to being captured in the sample.

The energy-dependent self-shielding factor $F(E)$ represents the correction for neutron flux attenuation due to interactions within the sample and is defined as

$$F(E) = \frac{1 - \exp(-\sum_i n_i \sigma_{tot,i}^D)}{\sum_i n_i \sigma_{tot,i}^D}. \quad (3)$$

This expression contains a summation over all nuclides i contributing to the self-shielding factor at energy E. The theoretical total yield Y is the sum of the contributions due to Y_c and Y_n,

$$Y(E) = \sum_k (\varepsilon_{c,k} Y_{c,k}(E) + \varepsilon_n Y_{n,k}(E)), \quad (4)$$

where $\varepsilon_{c,k}$ represents the detection probability for neutrons captured by nucleus k, and ε_n denotes the probability of a neutron both reaching the detector and generating a detectable signal. The yield $Y_{n,k}$ accounts for neutrons scattered by nucleus k within the sample that are subsequently captured in the detector system. These events generate a time-correlated prompt background indistinguishable from true capture events, thereby contributing to the measured yield. Sensitivity to scattered neutrons becomes particularly significant for resonances where the neutron width substantially exceeds the radiation width. As evident from the equations, the observed yield demonstrates dependence on both the capture and elastic scattering cross sections.

There are currently two different methods for analyzing NRCA data. The first approach utilizes ratios of measured resonance areas along with calibrated reference samples of known composition. This double ratio method[3] requires minimal knowledge of the underlying physics or instrumentation. The second approach employs an absolute determination method through least-squares fitting of resonance profiles.[3] This technique demands detailed information about the resonance parameters, neutron beam characteristics, and γ-rays detection system. The latter method implements resonance shape analysis using established fitting procedures (*e.g.*, SAMMY[13]).

2.2. Compton imaging

To achieve neutron resonance capture imaging, we have developed a total energy detection system that features γ-ray imaging capability (i-TED) based on the reported result in Ref. [11]. This system is a dual-layer Compton detector, enabling simultaneous spatial discrimination of γ-ray origins and measurement of neutron capture resonance peaks. Figure 1 illustrates the principle of a dual-layer Compton detector. The detection system comprises a scatter position sensitive detector (S-PSD) for initial γ-ray interaction localization and partial energy measurement (E_1), and an absorber position sensitive

detector (A-PSD) for complete energy absorption (E_2). The source position can be reconstructed through analytical back-projection when the detector geometry (including dimensions and detector-sample distances) is known a priori.

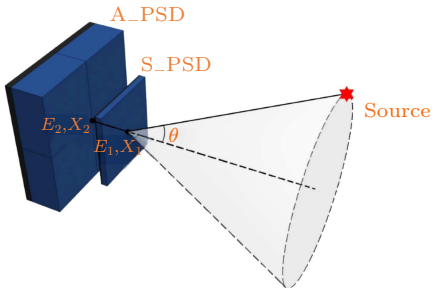


Fig. 1. Schematic diagram of dual-layer Compton detector.

The equation describing the intersection of the Compton cone with the sample is given by

$$\begin{aligned}&(n_x(x_s-a_x)+n_y(y_s-a_y)+n_z(z_s-a_z))^2\\&=\cos^2\theta((x_s-a_x)^2+(y_s-a_y)^2+(z_s-a_z)^2),\end{aligned}\tag{5}$$

where n_s are the components of a unit vector along the cone axis (the vector between the first and second interactions), as are the coordinates of the first interaction in the scatter detector, (x_s, y_s, z_s) is the position of the sample (true capture γ-ray source) and θ is the Compton scattering angle,

$$\cos\theta = 1+m_ec^2\left(\frac{1}{E_g}-\frac{1}{E_2}\right),\tag{6}$$

where E_g is the energy of the incident γ-ray, which is assumed to correspond to the sum of the energy in scatter detector E_1 and absorber detector E_2, c is the speed of light, m_e is the static mass of an electron, $m_ec^2 = 511$ keV.

Compton scattering imaging algorithms can be broadly divided into two distinct categories, which include analytical algorithms[14] and iterative reconstruction methods.[15–17] The most fundamental analytical approach is the direct back-projection algorithm. This method operates by systematically evaluating each voxel in the reconstruction space to determine its coincidence with back-projected Compton cones derived from detected events. The cumulative superposition of these conical projections generates the reconstructed image. In this work, given the preliminary stage of our current research, we adopted the back-projection algorithm, even though the uniform weighting of all cone-beam voxels inherently leads to streak artifacts.

3. Detector setup and characterization

3.1. Detector setup

First-generation Compton cameras primarily employed a double-layer structure composed of scintillator detectors.[18,19] With advancements in detector technology, semiconductor detectors have become the mainstream choice in Compton camera systems due to their superior characteristics, such as high detection efficiency, excellent energy resolution, and good linearity.[20,21] However, for the measurement experiment of neutron flight time, which requires fast time response, semiconductor detectors are unsuitable. In this work, $CeBr_3$ crystals are utilized due to their fast time response (< 100 ns) and good energy resolution. Additionally, in neutron capture reactions, the energy of cascade gamma rays can typically reach several MeV. $CeBr_3$ detectors are well-suited for such applications due to their broad energy response.

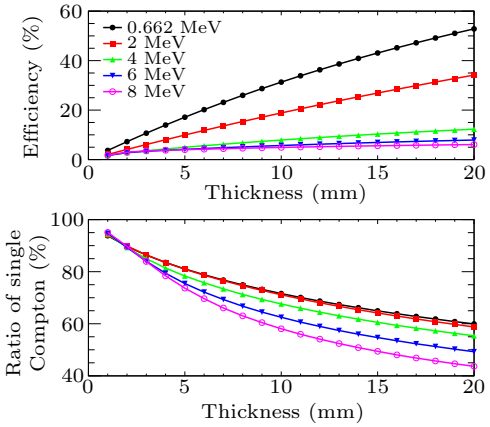


Fig. 2. The detection efficiency (top panel) and the fraction of single Compton scattering events (bottom panel).

The selection of crystal thickness is crucial. The thickness of the S-PSD crystal directly affects both the detection efficiency and positioning accuracy of the system. To determine the S-PSD crystal thickness, we investigated gamma-ray interactions and detection efficiency within individual scintillators. Using Geant4 simulations, we analyzed the single Compton interaction probability and detection efficiency for scintillators with thicknesses ranging from 1 mm to 20 mm, as shown in Fig. 2. The results cover gamma rays from 1 MeV to 8 MeV, demonstrating that while detection efficiency increases with thickness, the single Compton interaction probability decreases. This indicates the need to balance efficiency with positioning accuracy when determining crystal thickness. After comprehensive evaluation of both single Compton interaction probability and detection efficiency, we established 10 mm as the ideal thickness for the S-PSD crystal, while selecting 20 mm for the A-PSD to maximize performance. In addition, the performance of the detector is influenced by the distance between the radiation source and the S-PSD (d_s) and the distance between the A-PSD and the S-PSD (d_f). According to Ref. [22], both d_s and d_f affect the measurement of the maximum Compton scattering angle. To accommodate this, our detection system allows both d_s and d_f to be adjusted.

The detection system incorporates five $CeBr_3$ scintillator crystals. The $CeBr_3$ crystals, being hygroscopic, are housed in aluminum casings with optical glass output windows, where

rear-coupled SiPMs provide gamma interaction position. Figure 3 illustrates the assembly of an individual $CeBr_3$ scintillation crystal with its corresponding SiPMs. The SiPMs are composed of an 8×8 array of units, each with a sensitive area of 6.13 mm×6.13 mm. The crystal size for S-PSD is 5 cm×5 cm×10 mm, and the crystal size for A-PSD is 5 cm×5 cm×20 mm. These five crystal-SiPMs units are then integrated into a detector cell. The detector system primarily consists of an S-PSD, an A-PSD, readout electronics, and detector bracket, as illustrated in Fig. 4. Notably, the distance between the S-PSD and A-PSD is adjustable.

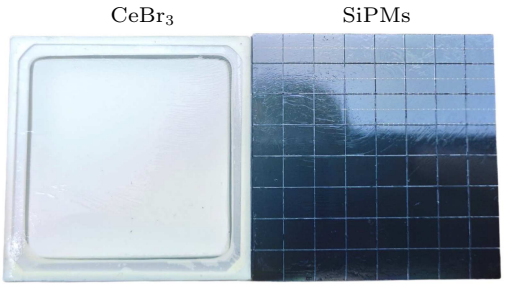


Fig. 3. $CeBr_3$ crystals and SiPMs.

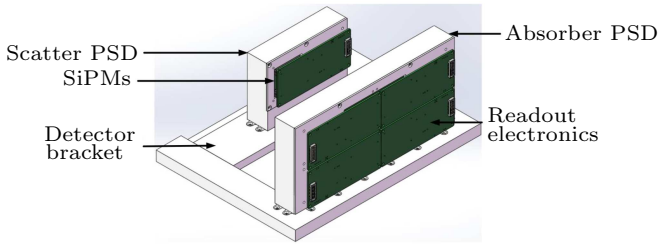


Fig. 4. Layout of NRCI detector in this work.

This readout electronics[23] employ the TOFPET 2C application-specific integrated circuit (ASIC) to process SiPMs signals. The digitized data from the ASICs are subsequently processed by a field programmable gate array (FPGA) before being transmitted to the backend system.

3.2. Detector characterization

The energy calibration was conducted using three radioactive sources (^{207}Bi, ^{60}Co, and ^{137}Cs) sequentially positioned 5 cm from the detector to ensure complete illumination. Both the S-PSD and A-PSD demonstrated excellent energy resolution performance, achieving a full width at half maximum (FWHM) of 5%–6% at 662 keV as quantitatively summarized in Table 1. The energy resolution of the detector under operating conditions (*i.e.*, with a 10-ns coincidence time window between S-PSD and A-PSD) was measured to be approximately 12% at 662 keV. The energy resolution curve was fitted with the function $\Delta E/E = \sqrt{A^2 + B^2/E + C^2/E^2}$, and the result is shown in Fig. 5(a).

The time resolution between the S-PSD and the A-PSD is crucial. We therefore placed a ^{60}Co source between the scatter and absorber detectors. The measurement results are shown in Fig. 5(b); the system demonstrates $\sigma = 667$ ps (FWHM ≈ 1.6 ns), confirming good time resolution characteristics.

Table 1. The energy resolution of the S-PSD and A-PSD.

Energy (keV)	S-PSD	A-PSD1	A-PSD2	A-PSD3	A-PSD4
570	6.25	4.87	5.56	5.66	5.43
1064	6.05	3.83	4.26	4.25	4.50
662	5.83	5.22	5.08	5.05	4.99
1173	6.24	4.19	4.35	4.18	4.46
1332	6.14	3.64	3.86	3.81	3.96

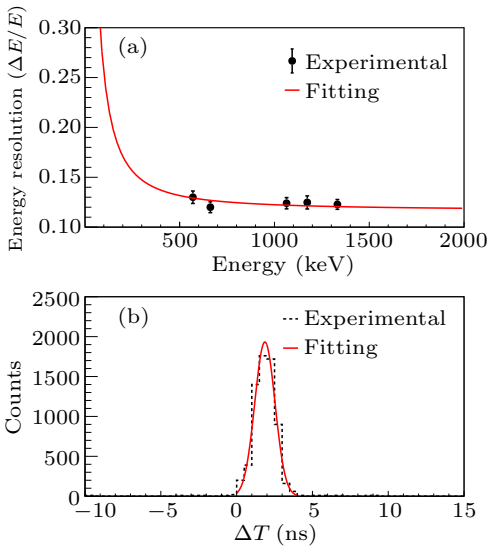


Fig. 5. (a) Energy resolution *versus* gamma energy and (b) time resolution.

In gamma-ray source imaging applications, accurate reconstruction of interaction coordinates for the primary γ-ray events within the scintillation crystal is essential. According to the signal integral of different pixels, the gamma incidence position can be reconstructed. The most common reconstruction techniques include the Anger logic method[24] and its variants, as well as the square charge centroid method.[25] In this work, we adopted a software-based Anger logic approach instead of hardware implementation. Although the Anger logic method has been surpassed in performance by advanced algorithms (*e.g.*, analytical models[26] and neural networks[27]), its simplicity makes it the fastest in computation. Thus, at the current research stage, the Anger logic is used to reconstruct the gamma incidence positions. The distance between the S-PSD and A-PSD in this detection system is adjustable. Through optimization balancing detection efficiency with angular resolution, d_f was determined to be 40 mm. For imaging tests, a ^{137}Cs reference source was positioned at 10 cm from the S-PSD. The coordinate system is set such that the X-axis corresponds to the horizontal direction, the Y-axis to the vertical direction, and the Z-axis to the direction of the detector. The source was positioned at three points relative to

the center: top-center (displaced 30 mm along Y), and top-right (displaced 30 mm along both X and Y). The filtered back projection algorithm[28] is used to image the gamma source at different locations. Figure 6 demonstrates successful image reconstruction with correct positional offsets for all three configurations, (a) central position, (b) top-center position, and (c) top-right position, while Figs. 6(d)–6(f) display the corresponding projection profiles for the center, top-center, and top-right configurations, respectively. Due to the influence of artifacts generated by the backprojection algorithm, the projection only conforms to a Gaussian distribution at the imaging position.

The projection profiles (as shown in Figs. 6(d)–6(f)) were analyzed via Gaussian fitting, giving $\sigma_x = 3.83$ cm and $\sigma_y = 3.75$ cm for horizontal and vertical resolutions. The measured center coordinates (X, Y) for the source at the center, top-center, and top-right positions were $(-0.54, 0.83)$ mm, $(-0.68, 17.18)$ mm, and $(17.70, 18.80)$ mm, respectively.

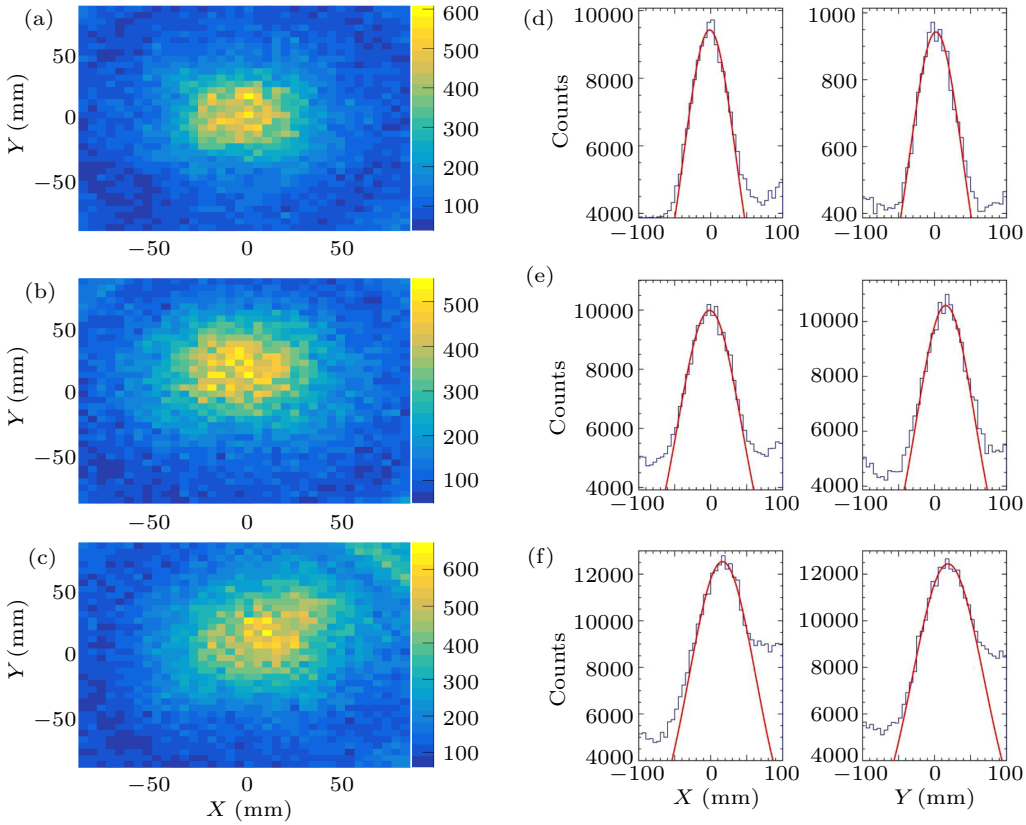


Fig. 6. Imaging results of ^{137}Cs: panel (a) corresponds to the center position, panel (b) corresponds to the top center, and panel (c) corresponds to the top right.

4. Detection system testing at Back-n

In this section, we describe the part of the work carried out at Back-n. The purpose of this measurement is to determine the reliability of the flight time measured with our detection system and the signal-to-background (S/B) ratio.[29] We first introduce the reader to the Back-n facility and then detail the measurements carried out with our detection system at the ES#2 of Back-n.

4.1. Introduction to the Back-n facility

The China Spallation Neutron Source (CSNS)[30,31] serves as a powerful neutron source for scientific research and industrial applications. Neutrons from CSNS are generated by slamming 1.6-GeV protons from the Rapid Cycling Synchrotron onto the spallation target with a 25-Hz repetition frequency. The present beam power of CSNS is 170 kW. Back-n,[32–38] which is mainly dedicated to supporting nuclear data measurements, detector calibrations, irradiation effect tests, *etc.*[39–54] Two experimental stations are located on the beam line at flight path lengths of approximately 55 m (ES#1) and 76 m (ES#2) from the spallation target. The Back-n beamline offers a wide neutron energy spectrum (0.5 eV–300 MeV), high flux (2.98×10^6 n/cm^2/s at 76 m from the spallation target), and low background. These features provide optimal beam conditions for applying neutron resonance capture imaging across a broad energy range, from eV to MeV.

4.2. Experimental setup

The present measurements are performed at the ES#2 experimental station. For time-of-flight measurement comparison, our detection system operated simultaneously with the C_6D_6 detector in neutron capture measurements, as shown in Fig. 7. The dimensions of the C_6D_6 detector and $CeBr_3$ detector are respectively Φ7.62 cm$\times$12.7 cm and a diameter of Φ38mm$\times$38 mm. The S-PSD of our detection system was

positioned approximately 17 cm from the sample, perpendicular to the beamline. This optimized placement represents the closest achievable distance that balances both imaging performance and beamline clearance requirements. The C_6D_6 detector was placed about 24 cm from the sample, also perpendicular to the beam. The $CeBr_3$ detector was located approximately 20 cm from the sample, with its axis at a 45° angle relative to the beam direction. The sample is placed at a distance of about 76 m from the spallation target. The C_6D_6 detector is characterized by a very low neutron sensitivity, but does not have spatial sensitivity. By contrast, our detection system is capable of imaging but has a very high neutron sensitivity, due to the bromine contained in the crystal, which has a quite high neutron capture cross-section dominated by resonances. The data acquisition system uses a CAEN DT5730B waveform digitizer for the C_6D_6 detector.

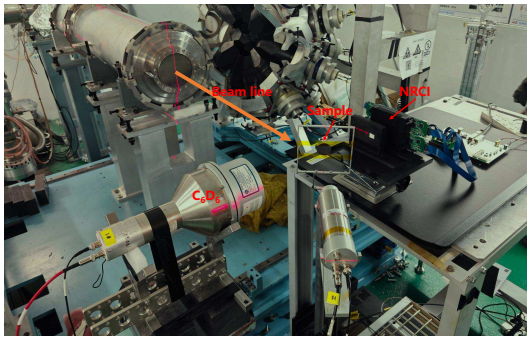


Fig. 7. Experimental layout at ES#2 of Back-n.

In this measurement, a disk of ^{197}Au 40 mm in diameter and 0.5 mm in thickness is placed at the target location. The sample was mounted at the center of the sample holder using Kapton tape. This stable isotope is chosen because its neutron capture cross-section is high, well-known, and standard, which is essential to extract reliable conclusions. To quantitatively evaluate the background, a filter was employed to remove neutrons of specific energies. After filtering out these neutrons, the black resonance filter (BRF) method was applied to assess the background and determine the S/B ratio. The filters used in this process included ^{nat}Cd, ^{59}Co, and ^{nat}Ta. Detailed information about the samples and filters is provided in Table 2.

Table 2. Sample and filters details.

Sample	Shape	Dimensions (mm)	Thickness (mm)	Purity (%)
^{197}Au	circular	40.0	0.5	99.9
^{nat}Ta	square	100.0	1.0	99.9
^{59}Co	square	100.0	1.0	99.9
^{nat}Cd	circular	80.0	1.0	99.9

4.3. Data processing

The time-of-flight is determined from the difference between the arrival time and a start time. In a capture experiment, the arrival time is obtained from the detection of the prompt γ-rays, which are emitted in the neutron capture reaction. At Back-n, the start time is provided by the γ-flash signal, generated in the detector mainly by the prompt γ-rays produced in the spallation process. The arrival time of the C_6D_6 detector is determined by the constant fraction discriminator (CFD) method. For the NRCI detector, after the time coincidence of the S-PSD and A-PSD, the time signal from the S-PSD is used as the arrival time. However, since gamma rays can trigger responses in multiple channels within the S-PSD, the arrival time is taken from the earliest responding channel. The time-of-flight spectra of the C_6D_6 and NRCI detectors are shown in Fig. 8. We observed dips at 4.28 eV, 10.34 eV, 132 eV, and 5.016 keV for ^{181}Ta and ^{59}Co filters, respectively. These dips help us evaluate the background in different energy regions.

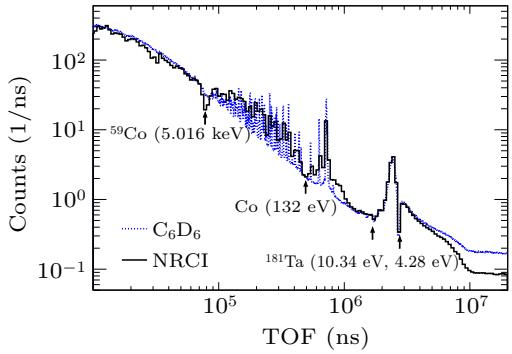


Fig. 8. The time-of-flight spectra of the C_6D_6 and NRCI.

This work involved measurements with an ^{197}Au sample and a without sample. The ^{197}Au sample was positioned at the center (0, 0, 0) mm. Using the filtered back-projection algorithm and the Anger logic method, we reconstructed images for both configurations, as shown in Fig. 9. The results demonstrate that, with identical acquisition times, the ^{197}Au sample yields significantly enhanced image contrast at the target position compared with the control measurement.

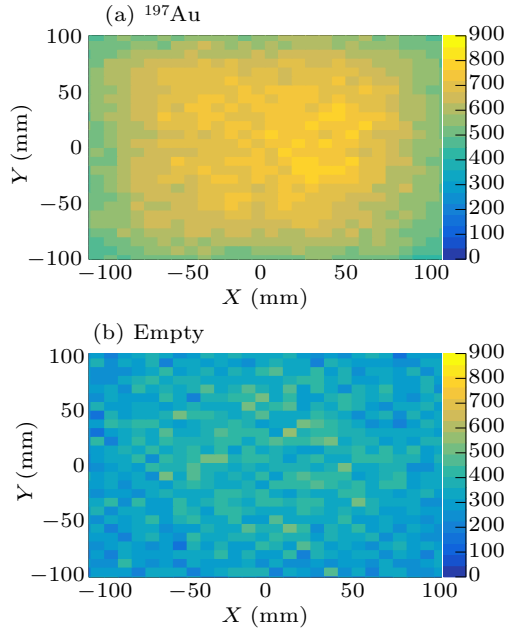


Fig. 9. Neutron resonance capture image (a) ^{197}Au and (b) empty over the full-energy region.

5. Results and discussion

The neutron energy is determined using the TOF method. At low energies, in the non-relativistic regime, the incident neutron energy (E_n) is determined with the TOF technique at the Back-n facility via the relation

$$E_n = \frac{1}{2} m_n v^2, \tag{7}$$

where the neutron velocity v is given by $v = L/t$, t is the time-of-flight that the neutron needs to travel a distance L, and m_n is the neutron rest mass. At high neutron energies, relativistic expressions must be used. Then the kinetic energy of the neutron is given as

$$E_n = m_n c^2 \left(\frac{1}{\sqrt{1-(v/c)^2}} - 1 \right), \tag{8}$$

where c is the speed of light. The neutron flight length L is 76 m from the spallation target to the surface of our detector. These curves in Fig. 10 represent the neutron energy spectra of our detector and C_6D_6 for the ^{197}Au sample. The blue dashed line represents the neutron energy spectrum measured by the C_6D_6 detector, while the black dashed line shows the neutron energy spectrum of NRCI detector for all imaging events. The red solid line indicates the neutron energy spectrum of NRCI detector for partial imaging events, the specific meaning of which will be elaborated in subsequent sections.

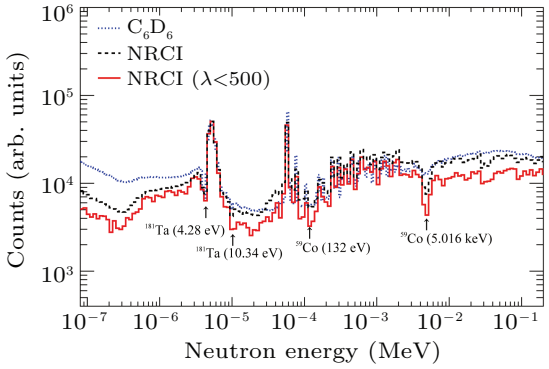


Fig. 10. The neutron energy spectrum for the ^{197}Au sample.

C_6D_6 is the most commonly used liquid scintillator material for NRCA measurements. Due to the extremely low neutron capture cross-sections of carbon and deuterium, it inherently exhibits very low neutron sensitivity. Therefore, when substituting the detection volume with other materials (especially inorganic crystals), this inherent neutron sensitivity naturally becomes the key concern. The neutron capture and scattering cross-sections of cerium and bromine are significantly higher than those of carbon and deuterium. However, the imaging capability of the detection system makes it possible to determine whether the registered radiation stems from capture in the sample under study, which may indicate a true capture event, or if it comes from the surrounding environment.[55–57]

To improve the S/B ratio, we adopt the parameter λ from Ref. [11], which is defined as

$$\lambda = (n_x a_x + n_y a_y + n_z a_z)^2 - \cos^2\theta (a_x^2 + a_y^2 + a_z^2) \tag{9}$$

from Eq. (5) can be employed. The sample position defines the origin of the coordinate system, *i.e.* $(x_s, y_s, z_s) = (0,0,0)$. The distribution of λ is shown in Fig. 11. Low λ values correspond to detected γ-rays that have a high probability of originating from the capture sample (true capture events). Conversely, high λ values correspond to events where the Compton cone does not overlap with the sample, thus indicating background events likely induced by neutron capture in surrounding materials or walls. The red solid line in Fig. 9 shows the neutron energy spectrum when $\lambda < 500$. According to the BRF method, the dips in the filters indicate the magnitude of background. Our detector shows consistency with the C_6D_6 at 4.28 eV for ^{181}Ta, and it demonstrates a better S/B ratio than the C_6D_6 detector at 10.34 eV for ^{181}Ta, 132 eV for ^{59}Co, and 5.016 keV for ^{59}Co. Using the 10.34-eV resonance dip of ^{181}Ta as a reference, the C_6D_6 detector achieved a signal-to-background ratio of approximately 10.2 at this energy. The λ-dependent variation of this ratio was characterized for our detection system, as presented in Fig. 12. As λ decreases, the signal-to-background ratio increases. While reducing the λ value improves the signal-to-background ratio, it must be noted that this simultaneously lowers detection efficiency due to the increased rejection of events. In this work, our detector demonstrated imaging performance and a favorable signal-to-background ratio in the eV energy range. These results indicate that our detector holds significant potential for achieving NRCI in the eV energy regime.

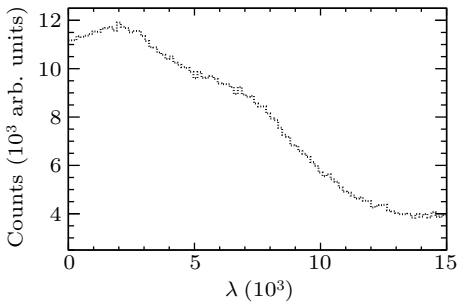


Fig. 11. λ-distribution for ^{197}Au sample.

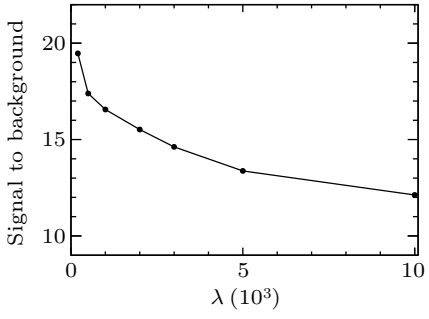


Fig. 12. Signal to background ratio *versus* lambda value.

6. Conclusion and outlook

This work developed an NRCI detector system, which is not only suitable for neutron resonance capture analysis but also capable of spatially resolved imaging. The imaging results showed $\sigma_x = 3.83$ cm and $\sigma_y = 3.75$ cm. Compton imaging and time-of-flight measurements of the ^{197}Au sample were conducted at the Back-n facility. There were significant differences between the empty sample and the ^{197}Au sample, which effectively reconstructed the position of the ^{197}Au sample. The background in the NRCI experiment was evaluated using the black resonance filter technique, demonstrating that our detection system has a better signal-to-background ratio in the same measurement. In addition, these measurements verified the performance of key detector components, including the SiPMs array and readout electronics system. Experimental results confirm that our detection system can implement NRCI measurements, with particular benefits for large-volume heterogeneous materials and archaeological specimen analysis.

The next step will be reducing dead materials and optimizing performance in terms of neutron sensitivity and algorithm. It is recommended to use inorganic crystals with lower intrinsic neutron sensitivity (*e.g.*, $LaCl_3$, YAP, and YSO scintillators). The imaging algorithm and gamma incidence position reconstruction algorithm used in this work are among the basic algorithms, and advanced machine learning approaches may be adopted in the future to improve performance.[58] Such a system would improve the accuracy of spatial cuts, thereby achieving a higher signal-to-background ratio and better imaging for superior NRCI measurements.

Acknowledgements

The authors are indebted to the operating crew of the CSNS Back-n white neutron source. Project supported by the Youth Talent Program of China National Nuclear Corporation, Natural Science Foundation of Inner Mongolia Autonomous Region, China (Grant No. 2025QN01029), University Basic Research Business Expense Project of Inner Mongolia Autonomous Region, China (Grant No. RZ2500000524), the Continuous-Support Basic Scientific Research Project (Grant No. BJ010261223282), the National Natural Science Foundation of China (Grant No. 11790321), and the Natural Science Foundation of Inner Mongolia Autonomous Region, China (Grant No. 2025QN01024).

References

[1] Postma H, Blaauw M, Mutti P, Corvi F and Siegle P 2004 *Journal of Radioanalytical and Nuclear Chemistry* **248** 115
[2] Postma H, Perego R C, Schillebeeckx P, Siegler P and Borella A 2007 *Radioanal. Nucl. Chem.* **271** 95
[3] Postma H and Schillebeeckx P 2009 *Encycl. Anal. Chem.* **2** 1183
[4] Schut P, Kockelmann W, Postma H, Visser D, Schillebeeckx P and Wynants R 2008 *Encycl. Anal. Chem.* **278** 151
[5] Schut P, Kockelmann W, Postma H, Visser D, Schillebeeckx P and Wynants R 2008 *Nucl. Instrum. Methods A* **505** 508
[6] Yao Y G, Xiao C J, Wang P S, Li C L and Zhou Q 2022 *Am. Chem. Soc.* **144** 5477
[7] Shuai D, Hong X Y, Guo L S, Zhang D P, Su B, Yan J Y, Guo J J, Li C L, Zhou Q and Wan B 2025 *Am. Chem. Soc.* **97** 12936
[8] Abdelnour R, Liu J T, K Hossny, A M. Wajid, Wenxin Li and Liu Z Y 2025 *Radiat. Phys. Chem.* **234** 112693
[9] Richard M and Zsolt R 2017 *Radioanal. Nucl. Chem.* **314** 843
[10] Cippo P, Borella A, Gorini G, Kockelmann W, Pietropaolo A, Postma H, Rhodes J, Schillebeeckx P, Schooneveld M, Tardocchi M and Wynants R 2010 *Nucl. Instrum. Methods A* **623** 693
[11] Domingo P 2016 *Nucl. Instrum. Methods A* **825** 076101
[12] Overley C, Chmelik S, Rasmussen J, Schofield S, Sieger E and Lefevre W 2006 *Nucl. Instrum. Methods A* **251** 6470
[13] Larson M 1985 *Office of Scientific & Technical Information Technical Reports* **1990**
[14] Shy D, Chen Z, Fessler A and He Z 2021 *IEEE Trans. Nucl. Sci.* **68** 211
[15] Richard G, Robert B and Herman T 1970 *J. Theor. Biol* **29** 471
[16] Rockmore J and Albert M 1976 *IEEE Trans. Nucl. Sci.* **23** 1428
[17] Wilderman J, Clinthorne H, Fessler A and Rogers L 1998 *IEEE Nuclear Science Symposium Conference Record* **3** 1716
[18] Schönfelder V, Hirner A and Schneider K 1973 *Nucl. Instrum. Methods* **107** 385
[19] Todd W, Nightingale M and Everett B 1974 *Nature* **251** 132
[20] Kamae T, Hanada N and Enomoto R 1988 *IEEE Trans. Nucl. Sci.* **35** 352
[21] Phlips F, Inderhees S, Kroeger R, Johnson W, Kinzer R, Kurfess D, Graham B and Gehrels N 1996 *IEEE Trans. Nucl. Sci.* **43** 1472
[22] Víctor B, Balibrea J, Caballero L, *et al.* 2019 *Nucl. Instrum. Methods A* **953** 163228
[23] Wang W Y, Cao P, Sun Z Y, Ren J and Wang J C 2025 *Nucl. Electron. Detect. Technol.* **45** 145
[24] Hal A 1958 *Rev. Sci. Instrum.* **29** 27
[25] Hal A 1966 *IEEE Trans. Nucl. Sci.* **13** 380
[26] Lerche C, Benlloch J, Sánchez F, Pavón N, Giménez N, Fernández M, Giménez M, Sebastiá A, Martínez J and Mora F 2005 *Nucl. Instrum. Methods A* **537** 326
[27] Li Z, Wedrowski M, Bruyndonckx P and Vandersteen G 2010 *Physics in Medicine and Biology* **55** 6515
[28] Wilderman S, Rogers W, Knoll G and Engdahl J 1998 *IEEE Trans. Nucl. Sci.* **45** 957
[29] Ren J, Ruan X C, Jiang W, Bao J, Luan G Y, *et al.* 2021 *Nucl. Instrum. Methods A* **985** 164703
[30] Chen H S and Wang X L 2016 *Nat. Mater.* **15** 689
[31] Huang M Y, Chen J X, Deng C, Huang T, Kang L, Liu H C, Lei L, Liu Y T, Qi X, Wang S, Wu Q B, Wu Y W, Xu S Y, Zhang W Q and Zhang Y L 2021 *12th Int. Particle Acc. Conf.* **15** 689
[32] Jing H T, Tang J Y, Tang H Q, Xia H H, Liang T J, Zhou Z Y, Zhong Q P and Ruan X C 2010 *Nucl. Instrum. Methods A* **621** 91
[33] Chen Y H, Luan G Y, Bao J, Jing H T, *et al.* 2019 *Eur. Phys. J. A* **55** 115
[34] Qiu Y J, Chen Y H, Li Q, Wang J C, Ren J, *et al.* 2025 *Nucl. Instrum. Methods A* **1075** 170383
[35] An Q, Bai H Y, Bao J, Cao P, Chen Y, *et al.* 2025 *JINST* **12** P07022
[36] Zhang L Y, Jing H T, Tang J Y, Li Q, Ruan X C, Ren J, Ning C J, Yu Y J, Tan Z X, Wang P C, He Y C and Wang X Q 2018 *Appl. Radiat. Isot* **132** 212
[37] Ren J, Ruan X C, Bao J and Luan G Y, *et al.* 2020 *Acta Phys. Sin.* **69** 172901 (in Chinese)
[38] Wang J C, Ren J, Jiang W, Ruan X C, Liu Y Y, *et al.* 2024 *Nucl. Sci. Tech.* **35** 164
[39] Li Q, Luan G Y, Bao J, Tang J Y, Jing H T, *et al.* 2019 *Nucl. Instrum. Methods A* **946** 162497
[40] Liu X Y, Yang Y W, Liu R, Wen J, Wen Z W, *et al.* 2019 *Nucl. Sci. Tech* **30** 139
[41] Chen Y H, Yang Y W, Ren Z Z, Jiang W, *et al.* 2023 *Phys. Lett. B* **839** 137832
[42] Ren J, Ruan X C, Bao J, Luan G Y, Huang H X and Nie Y B 2020 *EPJ Web of Conferences* **239** 17021

[43] Ren J, Ruan X C, Jiang W, Bao J, Wang J C, Zhang Q W, *et al*. 2022 *Chin. Phys. C* **4** 044002

[44] Hu X R, Liu L X, Jiang W, Ren J, Fan G T, Wang H W and Cao X G 2022 *Chin. Phys. B* **31** 80101

[45] Li X X, Liu L X, Jiang W, Ren J, *et al*. 2022 *Chin. Phys. B* **31** 038204

[46] Jiang B, Han J L, Ren J, Jiang W, Wang X H, *et al*. 2022 *Chin. Phys. B* **31** 060101

[47] Zhang Q W, Luan G Y, Ren J N, Ruan X C, al. 2022 *Acta Phys. Sin.* **70** 222801 (in Chinese)

[48] An Z D, Qiu W W, Jiang W, Yang G L, Li X K, *et al*. 2023 *Scientific Reports* **13** 12657

[49] Li X X, Liu L X, Jiang W, Ren J, Wang H W, Fan G T, *et al*. 2022 *Phys. Rev. C* **106** 045809

[50] Zhang S, Li G, Jiang W, Wang D X, Ren J, Huang M, *et al*. 2023 *Phys. Rev. C* **107** 045809

[51] Yijia Qiu, Changlin Lan, Yonghao Chen, Liyang Jiang, *et al*. 2023 *Phys. Rev. C* **107** 024606

[52] Pei B, Tan Z X, He Y N, Zhao X L and Fan R R. 2023 *Chin. Phys. B* **32** 020705

[53] Yue X P, Zhu Z F, Tang B, Huang C, *et al*. 2023 *Chin. Phys. B* **32** 090402

[54] Xue Y Y, Wang Z J, Chen W, Guo X Q, *et al*. 2023 *Chin. Phys. B* **32** 076101

[55] Pérez M, Caballero, Domingo P, *et al*. 2016 *Nucl. Instrum. Methods A* **823** 107

[56] Babiano S, Caballero, Calvo, Ladarescu,Olleros and Domingo P 2019 *Nucl. Instrum. Methods A* **931** 1

[57] Babiano, Balibrea, Caballero, Calvo, Ladarescu, Lerendegui, Mira P and Domingo P 2020 *Nucl. Instrum. Methods A* **953** 163228

[58] Babiano, Lerendegui M, J. Balibrea C, *et al.* 2021 *Eur. Phys. J. A* **57** 197